This is the author's final accepted version.

There may be differences between this version and the published version. You are advised to consult the publisher's version if you wish to cite from it.

http://eprints.gla.ac.uk/123123/

Deposited on: 22 August 2016

Accurate measurement of absolute experimental inelastic mean free paths and EELS differential cross-sections

Alan J. Craven, Joanna Bobynko, Bianca Sala and Ian MacLaren

SUPA School of Physics and Astronomy, University of Glasgow, Glasgow G12 8QQ, UK

ABSTRACT

Methods are described for measuring accurate absolute experimental inelastic mean free paths and differential cross-sections using DualEELS. The methods remove the effects of surface layers and give the results for the bulk materials. The materials used are $VC_{0.83}$, $TiC_{0.98}$, $VN_{0.97}$ and $TiN_{0.88}$ but the method should be applicable to a wide range of materials. The data were taken at 200keV using a probe half angle of 29mrad and a collection angle of 36mrad. The background can be subtracted from under the ionisation edges, which can then be separated from each other. This is achieved by scaling Hartree-Slater calculated cross-sections to the edges in the atomic regions well above the threshold. The average scaling factors required are 1.00 for the non-metal K-edges and 1.01 for the metal L-edges (with uncertainties of a few per cent). If preliminary measurements of the chromatic effects in the post-specimen lenses are correct, both drop to 0.99. The inelastic mean free path for $TiC_{0.98}$ was measured as 103.6±0.5nm compared to the prediction of 126.9nm based on the widely used Iakoubovskii parameterisation.

1. INTRODUCTION

A previous paper [1] demonstrated a technique to "extract" the electron energy loss spectroscopy (EELS) signal from precipitates contained in a thin sample of steel using DualEELS. DualEELS is a system for EELS that allows the low loss and core loss region of the spectrum to be recorded at each pixel of a spectrum image (SI) [2, 3]. This provides the complete energy range of the spectrum, allowing a more complete analysis of the resulting data. In particular, it provides the zero loss intensity. This allows: normalisation of the edge intensities; Fourier logarithmic deconvolution [4], which gives the single scattering distribution; and determination of the local thickness in terms of the inelastic mean free path (λ) [5].

Once the single scattering distribution has been obtained, the average shape of the matrix spectrum can be obtained from a region of the SI not containing a precipitate. On the assumption that the precipitate does not contain one or more major elements of the matrix, this matrix spectrum can be scaled and subtracted pixel by pixel from a region containing a precipitate in a way that reduces to zero those edge intensities present only in the overlying matrix. In this way, an SI of the precipitate contribution alone is "extracted".

In the single scattering distribution resulting from deconvolution, the following relationship applies:

$$I = \int \frac{dI}{dE} dE = NI_0 \int \frac{d\sigma}{dE} dE = N\sigma I_0 \qquad \text{1.}$$

where N is the number of atoms per unit area of specimen, I_o is the integrated zero loss intensity, dI/dE is the spectrum intensity divided by the channel width. I is dI/dE integrated over an appropriate energy window and σ is the partial cross-section obtained by integrating the differential cross-section, $d\sigma/dE$ over the same energy window. If $d\sigma/dE$ is known, then N can be determined.

If N is known at each pixel for each type of atom in the precipitate, then:

- the average composition of the precipitate at each pixel can be determined and hence any variations with position;
- the precipitate thickness at each pixel in the precipitate spectrum image can be determined using the low loss provided the inelastic mean free path is known;
- if the structure of the precipitate is known, the local chemical thickness (i.e. the number of atoms per unit area divided by the number of atoms per unit volume) can be determined pixel by pixel and compared to the total thickness obtained from the low loss region of the spectrum.
- from the local thickness, the volume of the precipitate can be determined.
- if the precipitate is viewed along a high symmetry direction and it possesses strong crystallographic faceting and symmetry, information on its probable shape can also be obtained.

All of this information is relevant to understanding the processing and properties of the material, in this case, a family of high manganese steels for automotive applications [6, 7]. For such information to be accurate, reliable values of $d\sigma/dE$ are required and obtaining them is the subject of this paper. In a subsequent paper, the values of $d\sigma/dE$ obtained here will be

combined with the spectra from some precipitates obtained in the previous paper [1] to give accurate quantitative data on precipitates.

Much of the quantitative work performed previously using EELS has used calculated differential cross-sections for this purpose. These are calculated using either the hydrogenic or the Hartree-Slater model [8-11]. Such cross-section calculations are based on isolated atoms and contain no information on the energy loss near edge structure (ELNES) or the extended energy loss fine structure (EXELFS) arising from the neighbouring atoms present in a solid. Nor do they include the white lines that arise when d or f states are close to the Fermi level, as in the transition or lanthanide series, although Rez and Rez have proposed a method of doing this [12]. An extension to the hydrogenic model seeks to include the effects of white lines using an empirical correction [11].

In addition, as the energy loss range normally accessible to EELS is a few keV, the core states that can be used vary with atomic number. For the light elements, the thresholds of the K-edges fall in the accessible energy loss range and the accuracy of these cross-sections are usually thought to be within a few percent [11]. Once the K-edges become inaccessible, the $L_{2,3}$ edges are used and the uncertainty in these is thought to be about 15%, at least for low collection angles [11]. This uncertainty is compounded by the presence of the white lines. When the $L_{2,3}$ edges become inaccessible, the $M_{4,5}$ edges are used and the uncertainty is these is even greater [11]. Again, white lines are an issue in the lanthanides.

Such theoretical cross-sections are widely used (for example, they are implemented in Digital Micrograph). Since the shapes of the calculated and experimental cross-sections do not match, the signal and the cross-section are integrated over an energy window before taking the ratio [11]. In most experiments where quantification has been performed, the value of I_o in Equation 1 has not been available. Thus N for each element cannot be obtained. However, the ratios of the values of N for the different elements can be determined, and hence the percentage of each element present can be calculated. The uncertainty in the calculated cross-sections should be considered to be an unknown systematic error. Thus if edges of the same type are involved e.g. two K edges, the uncertainty may be much lower than the uncertainty in the individual cross-sections, since the systematic errors should largely cancel. This benefit may not apply if the ratio of a K to L cross-section is involved.

Another approach is to use standards. Very good quality relative quantification has been achieved using a standards-based k-factor approach [13-23]. For this to work well, one of a number of situations is required:

- Both the sample and standards are rather thin (for example, the classic criterion is $t/\lambda < 0.3$ [11]) so that multiple scattering does not affect the integrated post-edge counts significantly. One recent study with relevance to our current work on (Nb,Ti) carbides showed an excellent example of this approach for the quantitative analysis of niobium oxides [22, 24].

- The sample and standards have similar values of t/λ, provided this is ≤ 1

- A low loss spectrum from the same area as the core loss spectrum is available to allow deconvolution of the multiple scattering. Without DualEELS, this is really only viable for "point" analyses rather than processing data from an SI.

Whilst it was possible to determine absolute differential cross-sections previously [20, 25, 26], in practice this was difficult and rarely performed due to the huge intensity difference between the bright zero loss peak and the weak core loss edges. Cross-sections, where measured, were usually calculated from the experimentally determined ratio of an intensity from the edge of interest to that of another edge with a better known cross-section (e.g. Manoubi et al. [17, 27], rather than by direct measurement. Neither method is particularly applicable to EELS mapping using spectrum imaging.

With DualEELS, it is now possible to obtain experimental differential cross-sections from well-characterised bulk material under conditions that can also be used for spectrum imaging with a resolution of a few Ångströms. Kothleitner *et al.* [26] have demonstrated the use of DualEELS for this. The current paper uses a similar approach, discusses the separation of edges, compares the experimental cross-sections to the calculated cross-sections in the atomic range and considers the random and systematic errors involved. Since this work is part of a project studying precipitates in high manganese steels, it uses VC, VN, TiC and TiN bulk ceramic standards to obtain differential cross-sections for the C K-, N K-, Ti $L_{2,3}$- and V $L_{2,3}$-edges. The experimental conditions used are those used in the earlier steel study.

Two key issues have to be addressed in order to obtain accurate differential cross-sections. The first is the fact that making thin samples from bulk material can change the material and, in particular, can cause a surface layer of significantly different composition to that found in the bulk. The second is that the absolute thickness of the sample must be determined accurately.

The surface layer problem is tackled by taking data over a range of specimen thickness and then using a least squares fitting technique to extract the bulk behaviour in a manner

similar to that used in earlier work by Mendis and Craven [28]. In this work, this is performed by plotting I/I_0 against N and determining σ or $d\sigma/dE$ from this. In order to calculate N at each point, an absolute value of the thickness must be determined.

To determine the local thickness from the value of t/λ obtained from the low loss spectrum, an accurate value of λ is required. A measurement of λ is carried out for TiC and the values for the other standards are obtained from it by using this to scale the parameterisation of experimental data by Iakoubovskii et al [29].

Taking a similar approach to Kothleitner et al. [26], a needle-shaped specimen of TiC is used. However, rather than look at a cross-section of the needle after the data are acquired to verify that it is circular, here a method is used which makes a direct measurement of the needle thickness during the experiment. A SI is taken at a given tilt and the corresponding HAADF image is taken after rotating the needle by 90° around its axis. Thus a value of t/λ from the SI can be matched directly to the thickness of the needle by measuring the width of this HAADF image. Data are also taken over a range of thicknesses so that the effects of any surface layer can be removed. In this way, λ can be determined directly and compared to that obtained from the Iakoubovskii parameterisation [29].

This parameterisation gives an improved fit to the data originally parameterised by Malis *et al.* [30]. Subsequent analysis by Zhang *et al.* [30, 31] showed that it performed very well for the high convergence and collection angles used in modern aberration corrected STEM instruments in general and this work in particular. It gave discrepancies of less than 2% with experimentally measured values for MgO. While we found a significant difference between the experimental and Iakoubovskii values for TiC, the parameterisation ought to give accurate relative values of the mean free paths for these closely related compounds and so be suitable for extrapolating the experimental value for TiC to the other standards.

2. THEORETICAL APPROACH
a. Deriving an Experimental Cross-Section from a Real Specimen

Some Ga ion implantation and some damage will always remain on the surfaces of a lamella or needle made using a focused ion beam (FIB) even after "polishing" with low energy ions. When the sample is removed from the FIB, it is likely that some oxidation of this surface layer will also occur. While the nature of the surface layer may vary with depth, it will eventually end, leaving the original bulk material. Due to its method of formation, this

layer will be essentially homogeneous across the surface of the lamella. Thus, provided that there is bulk material between the two surface layers on the sample, an increase in thickness will result in an increase of signal from the bulk but not from the surfaces. If the surface layers remain approximately normal to the electron beam, their contributions to the signal will be independent of position and so relatively easy to remove.
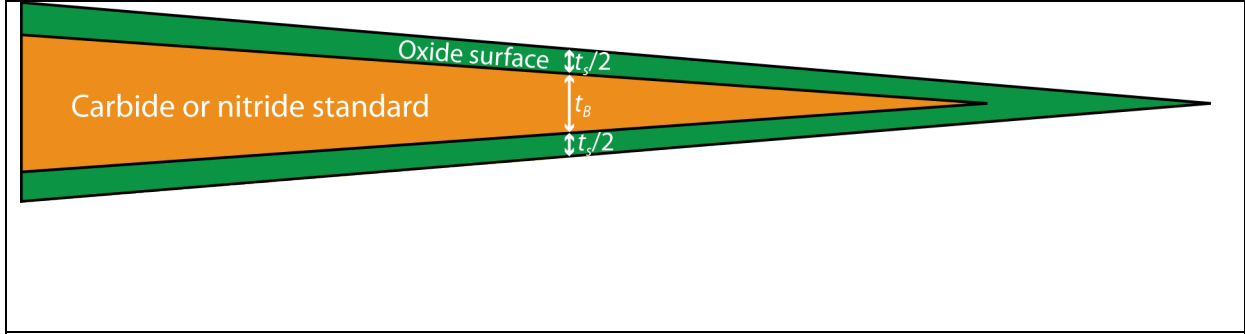

Fig 1　Schematic of a FIB Lamella

Figure 1 shows a schematic of such a sample where the total thickness of the top and bottom surface layers is t_S, which is taken as constant. The bulk material has a thickness t_B that varies with position. The corresponding inelastic mean free paths are λ_S and λ_B respectively. After deconvolution, the spectrum is a single scattering distribution and so the contributions from the surface layers and the bulk layer are additive. The number of atoms per unit area, N, is given by the number of atoms per volume, n, multiplied by the thickness, t. Hence the single scattering distribution can be written as

$$\frac{1}{I_0}\frac{dI}{dE} = \frac{1}{I_0}\left[\frac{dI_B}{dE} + \frac{dI_S}{dE}\right] = t_B \sum_i n_{Bi}\frac{d\sigma_{Bi}}{dE} + t_S \sum_i n_{Si}\frac{d\sigma_{Si}}{dE}$$

2.

where each sum is over both all components (atomic species) and all the electron states in those components, the first sum being for the bulk and the second for the surface layers. As long as the surface layers are homogeneous over the surface, the atoms need not be homogeneously distributed within its depth for the equation to be valid.

The left hand side of this equation can be measured experimentally and the values of n_{Bi} are known from the composition and structure of the bulk standard. The bulk thickness and the parameters for the surface layer are not known. However, the value of t/λ for the sample is available from the low loss and this can be expressed as

$$\frac{t}{\lambda} = \frac{t_B}{\lambda_B} + \frac{t_S}{\lambda_S}$$

<div align="right">3.</div>

Since t_S is assumed to be constant, $dt_B = \lambda_B \, d(t/\lambda)$, allowing the slope of a plot of $(1/I_0)(dI/dE)$ versus t/λ to be written as

$$\lambda_B \sum_i n_{Bi} \frac{d\sigma_{Bi}}{dE}$$

<div align="right">4.</div>

Thus by recording data over a range of thicknesses, processing to give a single scattering distribution and then taking the slope of the above plot using a least squares fit, the quantity in Equation 4 can be found at each energy in the spectrum from each pixel in the SI. This is true for both the low-loss and the core-loss regions of the spectra.

Here it is the core loss region that is of interest and, in particular, the two ionisation edges from a binary compound MX_x sitting on an approximately power law background from electrons in less tightly bound states. If the slope given in Equation 4 is normalised by $\lambda_B n_M$, where n_M is the number of M atoms per unit volume, Equation 4 can be written as

$$Background + x\frac{d\sigma_X}{dE} + \frac{d\sigma_M}{dE}$$

<div align="right">5.</div>

where all the terms from the excitation of lower lying states are grouped into the "Background". Equation 5 gives the absolute experimental cross-sections for the two elements of interest in the original bulk material with the artefacts introduced by the surface layers removed.

Removing the background from the two cross-section terms and then separating these two terms with sufficient accuracy are significant problems and this is discussed in detail below. As part of the process, Hartree-Slater (HS) atomic cross-sections are used. These are calculated using the routines in Digital Micrograph [8, 10]. A chemical shift is applied so that each calculated cross-section starts at the experimental edge threshold. The shifts are C - 2.0eV, N -4.0eV, Ti +0.5eV and V +0.5eV. While the HS cross-sections do not account for the ELNES and EXELFS, these effects become small at energies well above the threshold so that the experimental and HS shapes should converge in this region [8].

Thus, after removing the background under the non-metal cross-section, the non-metal HS cross-section can be scaled to the experimental cross-section in a region immediately in front of the metal threshold.   This provides both a method of extrapolating the non-metal cross-section beyond the metal threshold and a suitable background under the metal cross-section so that it can be extracted.   Once the metal cross-section is extracted, the metal HS cross-section can be scaled to it.   The scaling factor for the metal gives a direct measure of the agreement between the experimental and the HS cross-sections.   For the non-metal the extracted cross-section and the scaling factor must be corrected to full stoichiometry by dividing them by the value of x.

With the four standards investigated, two experimental cross-sections are obtained for each of the four elements allowing a consistency check.   With the cross-sections for the four elements, a good approximation to the cross-section of any ternary or quaternary compound of the elements can also be found.

b. Determining an experimental value for λ_B

The method of determining an experimental value of λ_B was outlined above and involves the use of an SI recorded at one needle orientation and an HAADF image recorded after the needle has been rotated by 90° about its axis.   This approach allows a needle with an "elliptical" cross-section to be used (since manufacturing a perfectly circular cross section needle at dimensions < 100 nm is very difficult).   From the SI, a t/λ map is obtained and a profile of t/λ is taken along the axial direction. At each axial point, the profile contains the maximum value of t/λ.   From the corresponding HAADF image at 90°, a profile of the needle thickness, t, along the axis is obtained.

In principle, overlying one profile over the other and taking the ratio should give a profile with constant value equal to λ.   In practice, a number of issues have to be addressed. The needle, like any sample prepared in the FIB and subsequently exposed to atmosphere, has a surface layer that is different from the bulk material of interest.   Fortunately, the HAADF images show that the thickness of the surface layers and their projected thickness along the needle are constant to a good approximation.   The pixel size in the SI used to measure t/λ is larger than that used for the HAADF image used to measure t and the data are recorded at different specimen rotations.   Thus there is uncertainty in the alignment of axial positions of

the t/λ and t profiles and the positions of the sampling points along the axis in the two profiles do not coincide.

If the plots of t and t/λ increased linearly with axial position, the solution would be straightforward. Taking the slopes of the plots would remove any offset in the axial origins, the effects of any constant surface effects and deal with the differences in sampling point positions. The ratio of the slopes would then give λ_B.

In practice, the profiles vary approximately as the square root of the axial position – i.e. the needle is somewhat blunted towards the tip, as is often observed when manufacturing tips, e.g. for atom probe tomography. This makes it difficult to take account of the origin shift and surface layers using plots against axial position. For the data obtained here, the most stable results are obtained by plotting of t^2 against $(t/\lambda)^2$ and taking the slope tips with other shapes may require other approaches. Here, the values of t are interpolated onto the sampling points of t/λ using a quartic fit to a plot of t^2 versus axial position. As will be seen below, good straight lines are obtained and the slope is relatively insensitive to the offset of the axial positions. In fact, the error in the fitted gradient can be minimised by varying this offset. Since such a plot is a straight line and, assuming a single surface layer of constant thickness, the relationship between of t and t/λ can be expressed as a straight line of slope, m, and intercept, c.

$$(t_B + t_s)^2 = m\left(\frac{t}{\lambda_B} + \frac{t_s}{\lambda_s}\right)^2 + c \qquad\qquad 6.$$

Differentiating this with respect to t and re-arranging gives

$$\lambda_B^2 = m\left[1 + \left(\frac{t_s}{t_B+t_s}\right)\left(\frac{\lambda_B}{\lambda_s} - 1\right)\right] \qquad\qquad 7.$$

Both of the terms in round brackets will turn out to be much less than unity and so λ_B can be written as

$$\lambda_B = \sqrt{m}\left[1 + \frac{1}{2}\left(\frac{t_s}{t_B+t_s}\right)\left(\frac{\lambda_B}{\lambda_s} - 1\right)\right] \qquad\qquad 8.$$

3. EXPERIMENTAL METHODS
a. Materials and Sample Preparation

Solid, polycrystalline ceramic specimens of TiC, TiN, VC and VN were chosen as the standards and used to determine the absolute differential cross-sections. These materials are all based on the rocksalt structure. The VN standard specimen was provided by Prof. Dr. W Lengauer of the TU Wien and its stoichiometry is $VN_{0.97}$ [32]. The TiC, TiN and VC were provided as bulk materials by Dr C Chatfield at Sandvik Coromant. Two of these have measured stoichiometries – $TiC_{0.98}$ and $TiN_{0.88}$. The VC_x was designated as having a high carbon content but no value of x was provided. Examination of selected area diffraction patterns showed ordering in good agreement with that found by Venables *et al.*[33] showing that it is in the V_6C_5 phase field of the phase diagram reported by Billingham *et al.* [34]. This phase diagram shows that x could lie in the range 0.76 to 0.85 if the material had been allowed to equilibrate at ~600°C before cooling. The minimum value of x increases approximately linearly with equilibration temperature until at ~1230°C the value of 0.83 for the compound is reached. It is likely that the equilibration was above 600°C and so the composition range is probably narrower. Below, a value of 0.83 is used.

All the standards were prepared for microscopy as standard FIB lamellae using a procedure similar to that used for the steel specimens [1]. The lamellae were cut from arbitrary directions in the polycrystalline materials and so have arbitrary orientations. Additionally, a TiC sample was prepared as a needle-shaped specimen by FIB using a procedure more normally applied to 3DAP specimen preparation [35].

b. Contamination minimisation

Since carbon is a key element in the precipitates of interest, it is essential to avoid carbon growth on the lamella and needle specimens during the acquisition time necessary to acquire high quality data. While the Dual-Beam FIB has oil-free pumping, the FIB preparation involves deposition of platinum using an organometallic precursor. To ensure that any residual precursor is removed along with any other adventitiously acquired hydrocarbon, all specimens are baked at 100°C either overnight or at least for several hours in a Gatan PIPS system, which also has an oil-free vacuum system. The high vacuum of the PIPS also prevents further oxidation of the specimen surfaces, something that is always a possibility if plasma cleaning with an Ar-O gas mixture is used e.g. when using a Fischione Plasma Cleaner. However, this plasma cleaner is used to clean the specimen holders for at least 3 minutes prior to using them. On removal from the PIPS, the specimen is immediately

loaded into the holder and inserted into the microscope. After this treatment, negligible carbon growth is normally observed and only data acquired under these conditions is retained.

The FIB lamellae are mounted in a JEOL double tilt holder (EM-01040RSTHB) and the TiC needle specimen is mounted in a JEOL high tilt tomography holder (EM-21310).

c. Equipment and parameters

All spectral data are recorded using a JEOL ARM200F operated at 200 kV and equipped with both a cold field emission gun as the electron source and a probe corrector. A Gatan GIF Quantum ER energy filter with fast DualEELS is used for the recording of the SIs. All SIs are recorded using the Digital Micrograph (2.x) software, with the scans under the control of Digiscan-2 hardware. For all SIs recorded in this work, a convergence half-angle of 29 mrad is used. The spot size is ~1 Å and the condenser settings are chosen to give a probe current in the range 180 to 400 pA. For EELS, the camera length is chosen so that the 2.5 mm aperture of the Quantum gives a collection half-angle of 36 mrad, resulting in high collection efficiency. A dispersion of 0.5 eV per channel is used.

d. SI acquisition conditions

A key requirement in choosing the acquisition conditions for recording the DualEELS SIs is that the two spectra can be spliced accurately. Because of the high intensity zero loss peak, the maximum integration time for the low-loss data set is kept short so that it remains in the linear region of the CCD response, and consequently the low-loss signal at the splice point is relatively low. Thus it is essential to maximise its signal-to-noise ratio and minimise any spurious contributions to it e.g. from stray scattering reaching the detector. The former can be improved by using multiple (5-10) integrations at each pixel and by keeping the splice point energy low. The stray scattering can be minimised by making sure that the zero loss peak is fully in the beam trap when recording the high loss signal. Nevertheless, the section of the CCD used for the low-loss signal continues to integrate the residual stray scattering during the longer high-loss integration time. Thus, keeping the ratio of the high-loss to low-low integration times (the time ratio) low minimises the contribution of the stray scattering to the low-loss signal. For this work, a time ratio of ~25 and a splice point of ~100eV proved to be optimum. This choice of splice point determines both the energy offset required for the high-loss spectrum and the integration time to keep the signal in the linear region of the CCD. Typically, there are 10 integrations per spectrum, each with an integration time of 200 μsec

for the low-loss and 5 msec for the high-loss taking 52 msec per pixel. With the readout overheads, this gives a recording time of 125 msec per pixel in the SI.

With these experimental conditions, the standard splice routine in DigitalMicrograph can be used with a 20 channel overlap to splice the low-loss and high-loss spectra. Ideally, the ratio between the high-loss and low-loss intensities in the splice region, the splice ratio, should equal the time ratio. However, this is not the case and the higher the time ratio the bigger the discrepancy. To confirm that the time ratio is the correct scaling factor, the same region of the spectrum was recorded in both the low loss and high loss channels for a range of time ratios. This shows that the signal ratios follow the time ratios to better than 1% and confirms that there is a residual contribution to the low loss signal which increase linearly with the high loss integration time. It is the latter that causes the splice ratio to be 6-10% lower than the time ratio in this work. However, the splice ratio is used to get a smooth join of the two regions for the purpose of deconvolution and the resulting signal is corrected in a subsequent stage of the processing.

To produce high quality data for the determination of cross-sections, SIs are recorded from areas containing a range of sample thickness. As discussed below, a range of values of t/λ from ~0.2 to ~0.8 proves to be ideal but the SIs are typically recorded with a larger thickness range and suitable sub-areas extracted at a later stage.

For the TiC lamella, SIs are recorded at several specimen orientations to verify that the large probe and collection angles to determine the conditions under which channelling effects modify the experimental cross-sections significantly. The orientations are:

- On a <110> pole (which would be expected to show the strongest channelling effects, as it has pure columns of Ti and C which have the closest spacing for any direction in this crystal structure):
- ~1° off this pole along a <110> Kikuchi line
- ~10° off this pole along a <110> Kikuchi line and in a two beam condition
- With an additional tilt of 3° perpendicular to this Kikuchi band and hence away from any strong Bragg condition.

For the TiC needle-shaped specimen, a SI and corresponding HAADF image of the tip are recorded at each orientation in a tilt series from -65$^{°}$ to +75$^{°}$ in 5$^{°}$ intervals. At each tilt, an HAADF survey image is recorded and a region at the end of the tip is selected for the SI.

12

The aim is to make this the same region at all tilts. Low loss and core loss SIs are recorded using DualEELS and the survey image is re-recorded to verify that specimen drift has not distorted the SI. The pixel size in the SI is 4.0 nm which is ~5 times that in the HAADF image (0.7nnm). At the larger positive tilts later in the series, the HAADF images show the onset of the growth of a thin carbon layer on the tip. As the scattering from amorphous carbon in the HAADF image is much less than that from Ti, the thresholding process described below excludes it from the measurement of t. However, it would be a more significant effect on the measurement of t/λ. Thus only 11 SI/HAADF pairs, covering the range from $-65°/+25°$ to $-15°/+75°$, are used in the analysis. The spectra in the corresponding core loss SIs verify that there is no change in the shape of the C K-edge due to amorphous carbon and hence that the t/λ used is valid. The STEM magnification used for the data collection is calibrated in the directions perpendicular and parallel to the rod axis using a MAG*I*CAL specimen[36], confirming that it is accurate to better than 1%.

4. ANALYSIS OF THE DATA, RESULTS AND DISCUSSION

a. Measuring the inelastic mean free path for TiC and extrapolating the result to the other standards
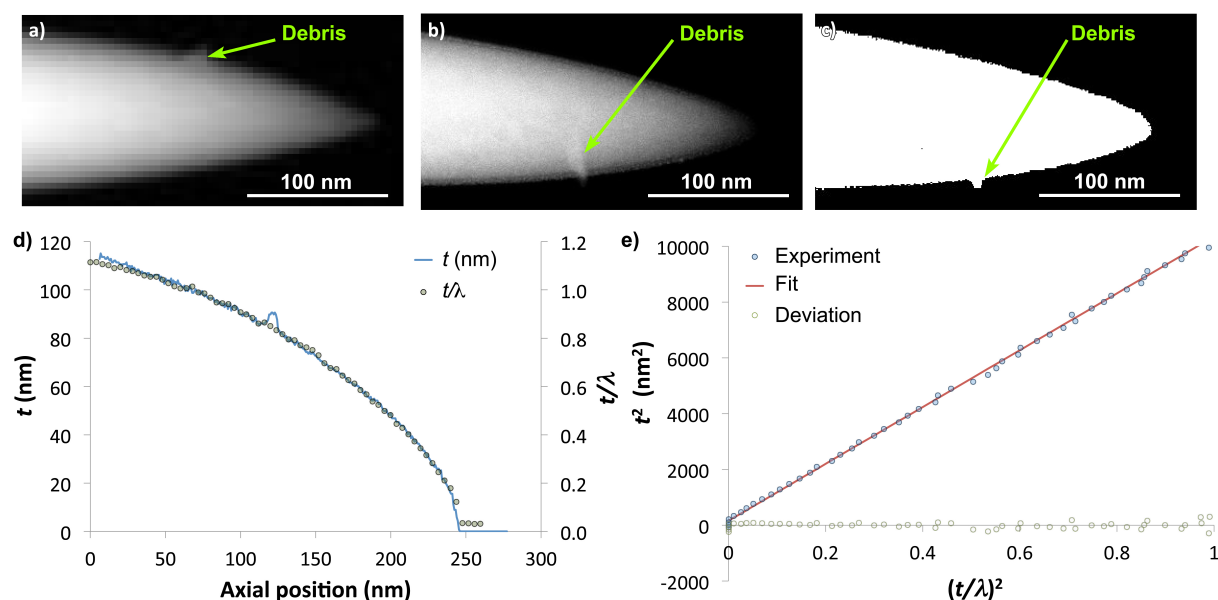

Figure 2. a) a map of t/λ from the TiC$_{0.98}$ tip; b) the HAADF image after rotating 90^0 about the tip axis: c) the HAADF image after thresholding; d) plots of maximum values t/λ in each vertical line of the image and the corresponding values of t from the HAADF image versus axial position (i.e. the horizontal direction, from left to right); e) a plot of t^2 against $(t/\lambda)^2$ together with a linear fit and the corresponding deviations.

Figure 2a shows the t/λ map from the 1st of the 11 SIs analysed and Figure 2b shows the corresponding HAADF image after the 90^0 rotation. This is taken from the region of the SI selected on the survey image at this new tilt. Thus a small difference in alignment is to be expected.

A small piece of debris can be seen in each. A script is used to identify the maximum value of t/λ in each vertical profile of the map and this is plotted as a function of axial position in Figure 2d. The presence of the piece of debris does not perturb the t/λ profile from this particular map as it is at the edge of tip. Thus the increased t/λ due to its presence never exceeds the value on the axis. However, as the tip is rotated about its axis to record subsequent SIs, the presence of the debris will eventually perturb the profile. When this happens, the positions where the perturbation occurs are excluded from the subsequent analysis.

The actual thickness of the needle at each axial position is given by vertical height of the needle in the HAADF image of Figure 2b. Since there is a big change in the signal level between the needle and the vacuum or any small amount of carbon contamination, the pixels where the needle is present can be identified by applying a threshold and setting the pixel to zero below the threshold and unity above the threshold, as seen in Figure 2c. A script was used to generate the thickness profile by summing the values in each vertical column of the thresholded image, scaling them by the pixel size and plotting them against the axial position. The t profile from Figure 2b is shown in Figure 2d after a shift of the origin determined by the subsequent processing. Here, the presence of the debris does perturb the profile because it goes outside the tip profile. Those positions where its effect is present are excluded from subsequent analysis. As the needle is rotated, the projection of the debris will eventually lie within the profile of the tip and so will no longer perturb the t profile.

t and t/λ follow each other closely in the centre section of Figure 2d and these points are used in the analysis. From the vertical scales, the mean free path is close to 100nm. Points very close to the tip are excluded because there is no bulk material present. Points where the graph of t becomes higher than that of t/λ in Figure 2c are also excluded. The reason for this deviation is not clear. EELS has always had an issue with values of t/λ in this region [37, 38]. It could also be an issue in the thresholding process used to measure t. As the diameter of the needle increases, the projected thickness of weakly scattering material at the edge

14

increases. Eventually the signal from this material will exceed the threshold and so becomes included in a measurement of the thickness.

As described in Section 2b, a quartic fit is used to interpolate the positions of the values of t onto the positions of values of t/λ. Figure 2e shows a plot of t^2 vs $(t/\lambda)^2$ together with a least squares linear fit and the corresponding deviations. The error in the fit has been minimised by adjusting the origin of the axial position of the t profile relative to that of the t/λ profile. Of the 11 pairs of data processed, the typical shift was 7 HAADF pixels, which corresponds to 1.4 SI pixels. The maximum shift was 20 HAADF pixels, corresponding to 3.5 SI pixels. Given that the regions of the SIs have to be set-up at each tilt, the small values of these positioning errors are an indication of the excellent reproducibility possible.

Ignoring the small correction term in Equation 7, the mean free path is given by square root of the gradient of the plot of t^2 vs $(t/\lambda)^2$. The error on each of the 11 values from the fits is <0.25%. However, the standard deviation of the 11 values is 1.6% indicating that other sources of random error are present (possibly some slight orientation effects, as discussed in section 4c with reference to figure 5).   Thus all values are treated as having equal weight giving a value of λ_B for $TiC_{0.98}$ of 103.6±0.5 nm.

Turning to the small correction factor in equation 8, since it is t^2 that is plotted, the slope of the graph will be dominated by the higher values of t and so an appropriate value to use in the first correction term is 100nm.   The total value of t_S can be measured from the HAADF images and is ~9nm.   The Iakoubovskii parameterisation can be used to compare the predicted value of the mean free path for $TiC_{0.98}$ of 127nm with those of oxides of titanium of which the surface layer might be composed.   Anatase has the largest value of 132nm with the others being much closer to that of $TiC_{0.98}$.   Thus the magnitude of the correction term in Equation 8 is ~0.002. Given that this is only an estimate and would result in a change below the standard error, no correction is made.

Table 1 gives the values of relevant parameters for each of the standards along with the mean free paths.   The lattice parameters are obtained using Vegard's Law to interpolate the data given by Goldschmidt [39] to the value corresponding to the composition of the standard. The values of n_M and the density, ρ, are based on this lattice parameter and the composition. ρ is to be used to find λ_B using the Iakoubovskii parameterisation [29].   The resulting values are not sensitive to the exact stoichiometries.

	TiC$_{0.98}$	VC$_{0.83}$	TiN$_{0.88}$	VN$_{0.97}$
Lattice parameter *a* (nm)	0.4328	0.4156	0.4239	0.4131
Metal atoms/ volume n_M (atoms/nm^3)	49.37	55.73	52.51	56.74
Density ρ (g/cm^3)	4.889	5.636	5.249	6.079
Iakoubovskii mean free path λ_B (nm)	126.9	122.6	124.7	120.3
Malis mean free path λ_B (nm)	97.7	95.7	96.5	96.4
"Experimental" mean free path λ_B (nm)	103.5±0.5	99.7±0.5 *	101.7±0.5 *	98.1±0.5 *

Table 1: Parameters for the standards, mean free paths predicted by Iakoubovskii et al.[29], Malis et al.[30] and the experimental mean free paths obtained by extrapolating the experiment value for TiC$_{0.98}$ using the ratios of the Iakoubovskii predictions. (* indicate extrapolated values).

The experimental value of λ_B for TiC$_{0.98}$ is significantly less than that predicted by the Iakoubovskii parameterisation [29] and is actually closer to that of the original Malis parameterisation[30]. However, the Iakoubovskii formula is used for extrapolation because of its use of density in the parameterisation. This gives a better fit to the same wide range of experimental data used by Malis *et al.*[30] in the original parameterisation. The mean free path for standard *MX* is obtained by assuming that $(\lambda_{MX}/\lambda_{TiC})_{expt} = (\lambda_{MX}/\lambda_{TiC})_{Iakoubovskii}$.

b. Obtaining spliced and deconvoluted datasets

The recorded SIs are processed using the procedure described in previous paper [1]. In short, both spectra are aligned in energy using the zero loss peak, any x-ray spikes are removed, channels containing no useful information are removed at either end of the spectra, and principal component analysis (PCA) is used for noise reduction using the plug-in for Digital Micrograph developed by Lucas *et al.* [40]. The difference between the SI before and after PCA is examined to detect any signs of bias or missing components. In the previous paper,

"bleed through" of intensity from the core-loss spectrum into the low-loss spectrum was a significant issue. However, following modifications to the QUANTUM system and using the improved acquisition conditions described above, it is much less significant. Thus the correction process used to correct for the "bleed through" and the smoothing of the low-loss prior to splicing are no longer required.   Finally the spectra are spliced and then Fourier log deconvolved.

From a t/λ map of the whole SI, one or more suitable sub-regions are selected in which the values of t/λ lie in the range 0.2 to 0.8. Equivalent sub-regions are extracted from the spliced SI and the deconvoluted SI. For use in later stages of the processing, maps of the splice ratio, S, are extracted from the former and maps of I_o is extracted from the latter.   For the sub-regions used the average splice ratio was 6 -10% less than the time ratio whereas in the earlier work it could be ~30% because the time ratio was larger and the stray scattering less controlled.

c.   Extracting the absolute experimental cross-sections

The value of the cross-section at each value of the energy loss (i.e. the quantity given by Equation 5) is found by using a least squares fit to take the gradient of a plot of $[(1/(I_0)_{xy})\,(I(E)_{xy}/\Delta E)\,(S_{xy}/T)]$ versus $[n_M\,\lambda_B\,(t/\lambda)_{xy}]$. λ_B is the "experimental" mean free path and n_M is the number of metal atoms per unit volume from Table 1. $I_{xy}(E)$ is the intensity of the spectra in the spatial pixel xy at energy E, and the plot is performed for all xy values in the spectrum image. S_{xy}, $(I_0)_{xy}$ and $(t/\lambda)_{xy}$ are the corresponding values in the maps of the splice ratio, the zero loss intensity and the relative thickness, as discussed in the previous section. ΔE is the energy width of the channels in the spectrum. T is the time ratio.   Thus the factor (S_{xy}/T) replaces the splice ratio used to splice the spectra with the time ratio in order to give the correct scaling between the core-loss and low-loss intensities.

To carry out the fits, a script was written in Digital Micrograph.   This script generates a spreadsheet of values of the points, fit values and deviations for each energy loss in the spectrum.   Plots of the differential cross-section and the corresponding errors from the least squares fits as a function of energy are also generated.   It should be noted that an 8-byte word length in Digital Micrograph is required to give sufficient accuracy in the least squares fitting routine.   With this word length and the sizes of the SI sub-regions used (less than 2000

pixels), the values of the fit parameters match those from the linear regression routines in Microsoft EXCEL. The onset of rounding errors in the least squares fit will set a limit to the maximum number of pixels that a sub-region can contain.

To demonstrate the effectiveness of the procedure in removing the contributions from surface layers, Figure 3a compares the $TiN_{0.88}$ cross-section with spectra summed in 5 x 5 pixel regions in the thickest and thinnest region of the SI. The data have been scaled to match in the window over the N K-edge. This was an early specimen with significant surface oxidation. Thus, in addition to the N K-edge, the $Ti_{2,3}$-edges and the Ti L_1-edge, there is a clear O K-edge in the spectra but not in the cross-section. The Ti signal is also relatively larger in the two spectra. If the scaled cross-section is subtracted from a spectrum, the result should be the spectrum from the surface layer. This surface signal should be the same in absolute terms in both the thin and thick regions if the assumptions made about it are true. Figure 3b shows the surface layer spectra from the thin and thick regions on an absolute scale. This confirms that they are almost identical so that the assumptions are valid and demonstrates the effectiveness of the approach in extracting the bulk signal from the SI.
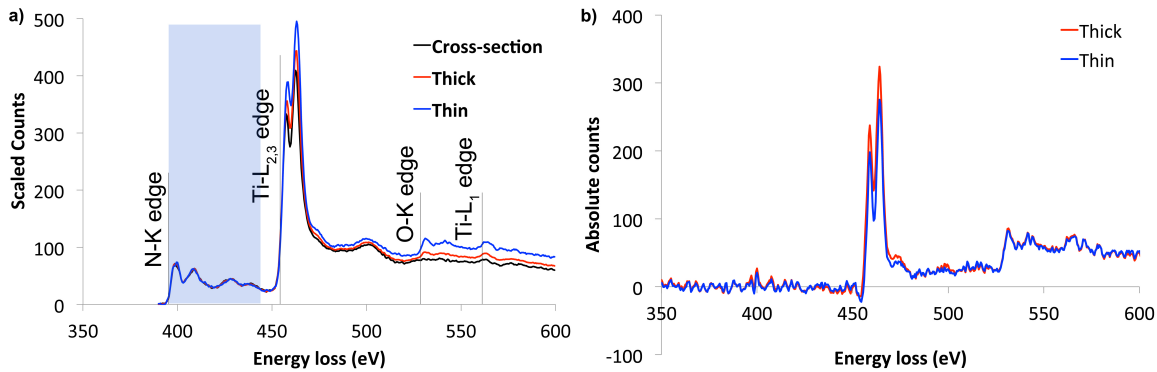

Figure 3. a) Comparison of the extracted cross-section of $TiN_{0.88}$ with spectra summed in 5x5 pixel regions in the thinnest and thickest regions of the SI. The data have been scaled to match in the window shown. In addition to the N K-, Ti $L_{2,3}$- and Ti L_1- edges, the spectra from the SI show a significant O K-edge but this is absent in the cross-section. b) The surface contributions, on an absolute scale, obtained by scaling and subtracting the cross-section from the spectra.

To demonstrate the quality of the least squares fits, Figure 4 shows plots of $[(1/(I_0)_{xy}) (I(E)_{xy} /\Delta E) (S_{xy}/T)]$ versus $[n_M \lambda_B (t/\lambda)_{xy}]$ from a $TiC_{0.98}$ lamella. The energy of the data in Figure 4a is the energy of the Ti L_3-peak, where there is a high intensity, while the energy of the data in Figure 4b is just before the Ti $L_{2,3}$-edge where there is a low intensity in

18

the spectrum.   Hence the vertical scales are an order of magnitude different.   It is clear from the deviation plots that the data are well fitted by straight lines.   In general, this is true provided that $0.2<t/\lambda<0.8$.   It is assumed that, at lower thicknesses, surface effects play too large a role to allow the straight line fit to continue.   As noted above, issues with values of t/λ > 1 have been known for a long time [37, 38].   At these higher thicknesses, there may also be issues with the Fourier-log deconvolution process or with inelastic scattering modifying the image contrast after energy loss relative to that in the elastic image (I_o), which is used to normalise the data.
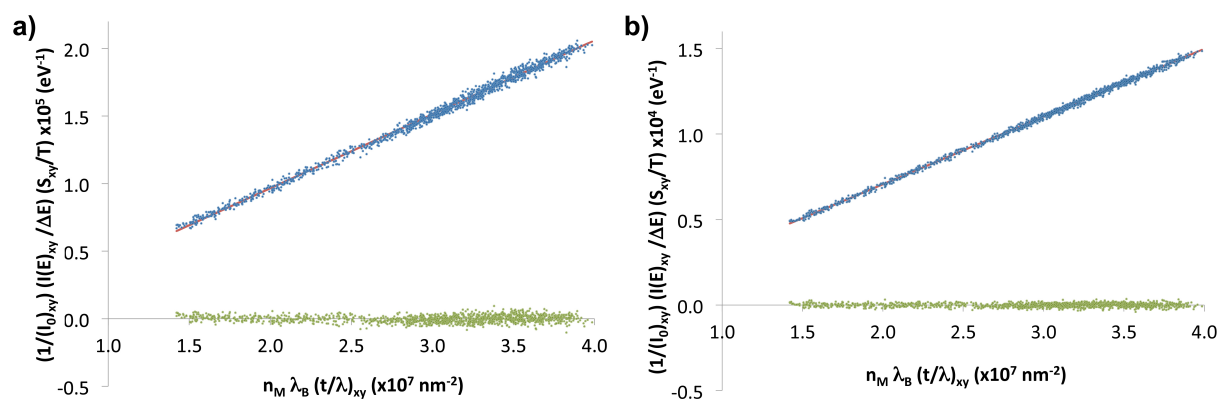
Figure 4.   Plots of $[(1/(I_0)_{xy})\, (I(E)_{xy}\,/\Delta E)\, (S_{xy}/T)]$ versus $[n_M\, \lambda_B\, (t/\lambda)_{xy}]$ for two values of energy in a TiC data-set:, a) at the energy of the Ti L_3-peak, where the signal is high, and b) an energy immediately before the Ti $L_{2,3}$-edge, where the signal is low.   Note that the vertical scale in b) has been increased by an order of magnitude relative to that in a).   In both cases, the actual data points are plotted in blue circles, the fit as a straight line and the residuals in green circles.

To investigate the effects of diffraction conditions and channelling on the cross-sections when using large probe and collection angles, cross-sections were measured on a $TiC_{0.98}$ lamella at the four diffraction conditions described in Section 2d.   Figure 5a compares these cross-sections.   The datasets used for these cross-sections were taken before the optimum acquisition conditions were determined and so there are minor differences in the background shape at the left hand edge due to issues with the splicing but, overall, the agreement is excellent.   Thus it appeared that channelling has little effect on the cross-sections and the final data was taken from the randomly oriented lamella without recording diffraction patterns to determine the precise diffraction conditions.

However, in responding to points raised by the referees, a more critical comparison is made in Figure 5b.   The two cross-sections recorded far from the <110> pole and significantly off the <110> two beam-condition are the least affected by channelling effects and their mean is used as a baseline.   The percentage deviations of the cross-sections from this baseline are shown as a function of energy loss in Figure 5b.   The percentage deviations of these two cross-sections must be equal and opposite and will show no significant variation with energy loss, as seen in Figure 5b.   These also indicate the level of deviation that just comes from noise in the datasets (about 1%). The percentage deviation of the cross-section recorded at the <110> 2-beam condition is slightly large but also shows no significant variation with energy loss, suggesting no significant channelling effects are present at such orientations.

However, the two cross-sections recorded in the vicinity of the <110> pole show significant variations with energy loss including a noticeable step across the Ti $L_{2,3}$-edge. This suggests that small but significant channelling effects may be present in such orientations.   Thus a more detailed investigation of this will be made in the future.

Given that the lamella orientations are random, it is unlikely that most orientations used in the data are close to low index poles.   As such it is unlikely that channelling effects make a significant modification to the results presented here, although deviations up to about 5% due to channelling effects cannot be completely ruled out.
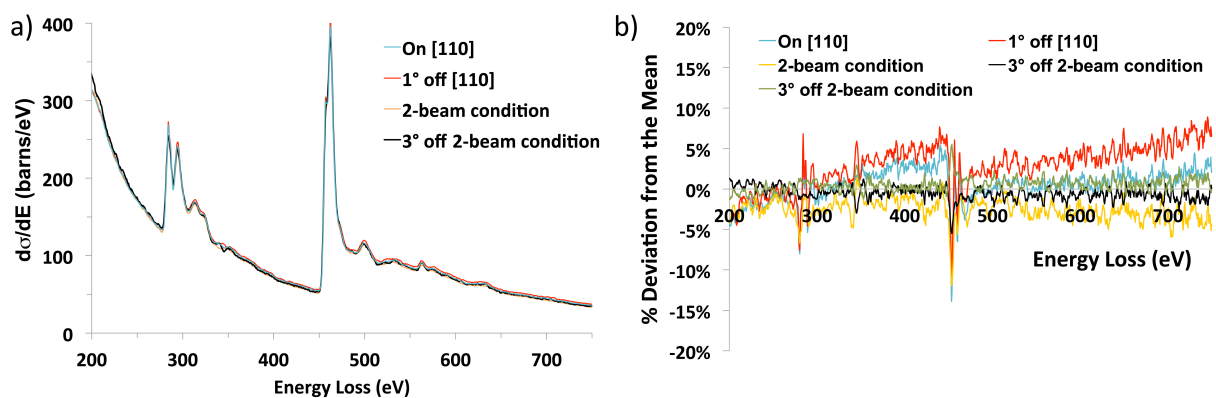

Figure 5   a) Comparison of 5 cross-sections extracted from a TiC$_{0.98}$ lamella each recorded at a different tilt.   b) Percentage deviations of the cross-sections from the mean of two datasets recorded 3° off the 2-beam condition

Having established the optimum conditions for acquisition, the data were re-taken. The numbers of sub-regions analysed is 10, 8, 6 and 6 for $VC_{0.83}$, $TiC_{0.98}$, $VN_{0.97}$ and $TiN_{0.88}$ respectively. The sub-regions contained between 600 and 1800 spatial pixels. The fractional standard errors in the slopes, i.e. the fractional standard error in the differential cross-section at the particular energy, was in the range from 0.1% to 0.4% over the majority of the energy range, being largest where the cross-section is lowest. There were peaks up to ~1% in the region of sharp features. The exception was one $TiN_{0.88}$ dataset where the fractional errors were 0.7-1.0%. Such low values are obtained because there are large numbers of spatial pixels in the SI sub-region from which the data is taken. Some plots show slight deviations from linearity giving systematic errors of 1-2% and such systematic errors, if present, will tend to dominate.

For each standard, the cross-sections were averaged and the fractional standard errors calculated at each energy. These were in the range 0.7% to 1.0%, with the higher values at the lower cross-sections and peaks above this near sharp features. These fractional errors are above the values on the individual cross-section measurements. Thus, as with the values of λ above, there are additional random errors in the measurements.
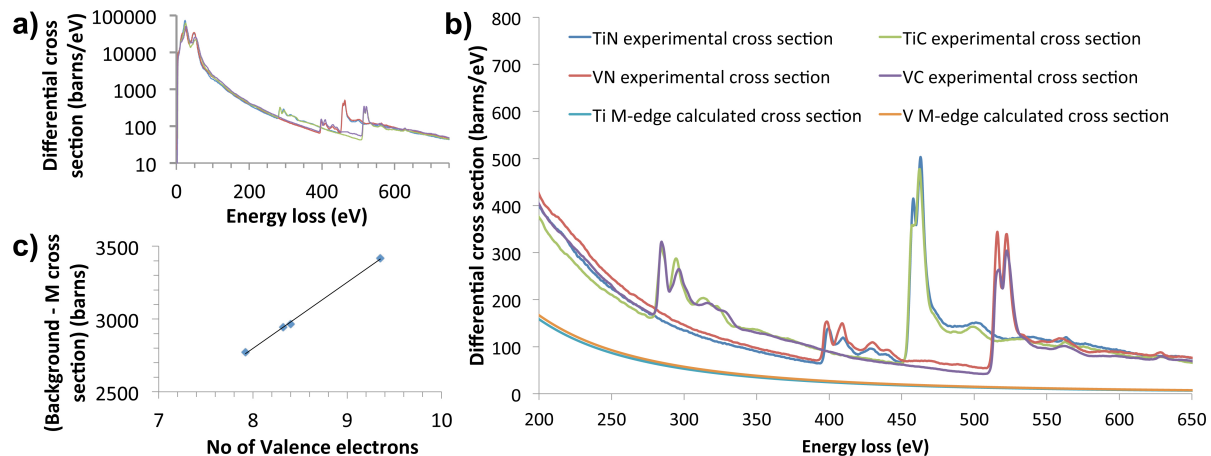

Figure 6 Comparison of the cross-sections extracted from the four standards. a) the whole energy range with a logarithmic intensity scale; b) in the region of the edges with a linear intensity scale. Also shown in b) are the HS M cross-sections for Ti and V. c) The valence electron partial cross-section plotted against the number of valence electrons. This is obtained by taking the difference between the experimental background cross-section and the relevant metal M cross-section and integrating the result from 251eV to 276eV.

Figure 6a compares the average cross-sections extracted from the 4 standards over the energy range from 0 to 750eV with a logarithmic intensity scale. N.B. because the

conversion from scaling by the splice ratio to scaling by the time ratio was applied over the whole energy range, the low-loss section is too low by 6% – 9% in this plot. The plot shows the excellent consistency of the extracted cross-sections over the whole energy range.

Figure 6b makes the comparison in the region of the core edges of interest. In the region prior to the C K-edge threshold, the backgrounds have structure that is reproducible and is likely to be due to EXELFS resulting from metal M shell excitations. The background from $TiC_{0.98}$ has the lowest intensity while that from $VN_{0.97}$ has the highest with those from $TiN_{0.88}$ and $VC_{0.83}$ being intermediate and similar. This is to be expected as the background will depend on the number of less tightly bound electrons and this number changes in the same way as the background intensities. 8 of these electrons are in the $M_{2,3}$ and M_1 shells of the metals and their HS cross-sections, as calculated by Digital Micrograph, are also shown in Figure 6b. The rest are valence electrons. Fully stoichiometric C, N, Ti, V should contribute 4, 5, 4, 5 valence electrons respectively. If sub-stoichiometric, those from C and N are scaled by the value of x in MX_x. The difference between the experimental background cross-sections and the corresponding HS M cross-sections should be the cross-section for the valence electrons. In Figure 6c this difference, integrated from 252eV to 276 eV, is plotted against the number of valence electrons in the standard. To a good approximation, this is a straight line. This would be expected as the excitation of valence electrons to such a high energies tends to a single electron excitation process as opposed to the collective excitation process at lower energy losses. The behaviour of the backgrounds gives confidence that the extraction of the cross-sections has not been perturbed by the residual stray scattering as had been the case before the optimum acquisition conditions were established.

d. Fitting Backgrounds and Hartree-Slater atomic cross-sections

To make use of the cross-sections for the individual elements, the background must be removed and the edges separated. This is always challenging when there are perturbations to the backgrounds e.g. from extended energy loss fine structure (EXELFS). Consequently, using the standard approach of fitting AE^{-r} in a window in front of the non-metal edge gives an extrapolated background that is sensitive to the position and width of the fitting window, and thus leads to inconsistent results. To try to overcome this, an extended version of constrained background fitting method proposed by Steele et al. [41] was tried. Here the experimental cross-section is modelled as the sum of a power law background, a scaled HS

non-metal cross-section and a scaled HS metal cross-section.   Three fitting windows are chosen, one prior to the non-metal edge, one prior to the metal edge and one well above the metal edge.   The square deviations in three windows are summed and this sum is minimised by varying the power law parameters and the two scaling factors.   The investigations showed that this approach worked.   However, there are no well-defined criteria for choosing the three fitting windows and the results are sensitive to this choice, sometimes significantly so.

Thus another approach is adopted.   The overall shape of the backgrounds in the four standards is very similar.   The deviations of the background from a power law fit are least in the Ti containing standards and the background in $TiN_{0.88}$ reaches to the highest energy loss before encountering a non-metal edge.   Fitting a power law background in a 20eV window prior to the N K-edge and using it to extrapolate the experimental $TiN_{0.88}$ background provides an "experimental background shape" that can be used with all four standards, if suitably scaled.   Here a scaling window 20eV wide in front of the non-metal edge is used. The average cross-sections and the scaled backgrounds are shown in Figure 7.   Also shown are the HS cross-sections added to the scaled background.   Those for the non-metals are scaled by the stoichiometry, x but those for the metals are unscaled.   The deviation of the experimental cross-section from the sum of the background and the two HS cross-sections is also shown.
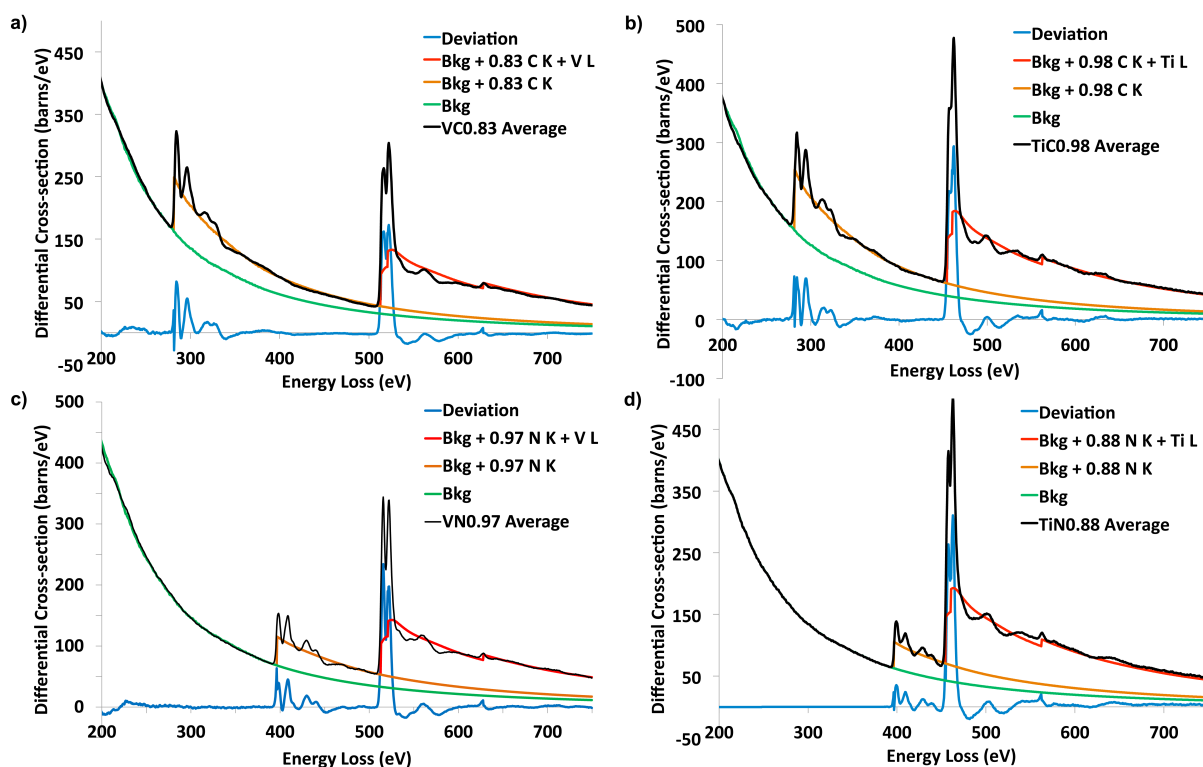

23

Figure 7 Comparison of the average experimental cross-sections, the scaled "experimental" background and the HS cross-sections. a) $VC_{0.83}$; b) $TiC_{0.98}$; c) $VN_{0.97}$; d) $TiN_{0.88}$. For a), b) and c) the experimental background shape described in the text has been scaled to match in a 20eV window before the non-metal edge. In each case, the HS non-metal cross-section is scaled by x, the stoichiometry but the metal HS cross-section is unscaled.

The "experimental background shape" fits very well. The deviations up to ~280eV are similar in $VC_{0.83}$, $TiC_{0.98}$ and $VN_{0.97}$. (There are no deviations in this region for $TiN_{0.88}$ since this was the source of the background shape.) Between 280eV and 390eV, the deviations in $VN_{0.97}$ are very small, giving some support to the use of this "experimental background shape". The noticeable deviations at lower energies are likely to be the differences in the EXELFS from the strong M edges of the metals at about 40-50 eV. The shape of the EXELFS are controlled by both the threshold energies of these edges and the lattice parameters and so will differ in the four standards.

The deviations in the region before the metal edges and well above them are also small. The exception is before the Ti edge in $TiN_{0.88}$ where the two edges are close together. Thus the experimental and HS cross-sections are in good absolute agreement in the "atomic region" well above threshold. However, these low deviations only occur from above ~100eV above the threshold in these compounds, which is much higher than figures quoted previously e.g. by Ahn and Rez [42] who compared experimental and calculated cross-sections by "*normalising them some 10eV above threshold where the intensity can be solely attributed to continuum transitions*". The agreement obtained in the current work also confirms both stoichiometries of the standards and the accuracy of the experimental mean free paths used in the extraction of the cross-sections.

At this point, it is worth noting that the deviations from the HS shapes caused by the ELNES are positive for the non-metals and negative for the metals. In these compounds, the hybridisation of the metal and non-metal orbitals increases the non-metal p-DOS, resulting in the sharp peaks close to the thresholds of the non-metal edges e.g. Paxton *et al*. [43]. Looking at the partial DOS presented in Figure 3 of that work, the metal d-DOS drops below the non-metal p-DOS for losses a few eV above the Fermi level and continues to be so up to beyond the 13.5 eV limit of that figure. If this behaviour continues to higher energy losses, it may explain the behaviour observed in the current paper. Unfortunately, at such high

energies above the Fermi level, density functional calculations become less accurate and so this has not been pursued.

It is now possible to extract the cross-sections for the individual edges, correct those for the non-metals to values corresponding to full stoichiometry and to compare the pairs of cross-sections obtained. This comparison is made in Figure 8. For the non-metals, the region at higher energy loss is not shown as this is the region where the cross-sections are extrapolated using the appropriated HS cross-section. Overall, the agreement is very good. For the non-metals in Figures 8a and b, the ELNES is similar in shape and intensity as expected from these essentially isostructural compounds but the energies of the features differ because the lattice parameters differ.

In Figure 8a, the shape of the carbon K-edge from thin amorphous carbon is shown for comparison. This has not been calculated as a cross-section but is simply presented as the background subtracted, single scattering intensity scaled to the HS cross-section in the region from 350 to 500 eV. The shape is in good agreement with the HS cross-section above ~300eV. Below this, the shape peaks above the HS cross-section in a manner that is similar to the other cross-sections. Amorphous carbon is a light, monatomic material where the ELNES and EXELFS are much less pronounced and where there can be no channelling effects. Thus the excess intensity of the shape over the HS cross-section after the threshold cannot be caused by such effects The edge shape is taken from spectral without the spectral data being taken through the cross-section extraction process. Thus the excess intensity is not caused by this process. The presence of this excess intensity in the case of amorphous carbon provides strong support for the observation of a significant excess experimental cross-section over a significant energy range after the non-metal threshold.

For the metals in Figure 8c and d, the ELNES is less strong and the agreement between the pairs of cross-sections is even better. All converge well to the corresponding HS cross-section at well above the threshold but, as noted above, are below the HS cross-section in the region after the threshold.

If the experimental N K-edge cross-section from $TiN_{0.88}$ is spliced to the HS cross-section immediately in front of the Ti L-edge, there is a sharp step as seen in the thin green line in Figure 8b. This is because there is a large dip from the ELNES at this point. A better approximation to the true shape can be obtained if a section from the N edge cross-section from $VN_{0.97}$ is inserted with a small energy shift so that it gives a smooth splice. This has

been done in the corrected spectrum discussed below and is shown as the thick green line in Figure 8b.
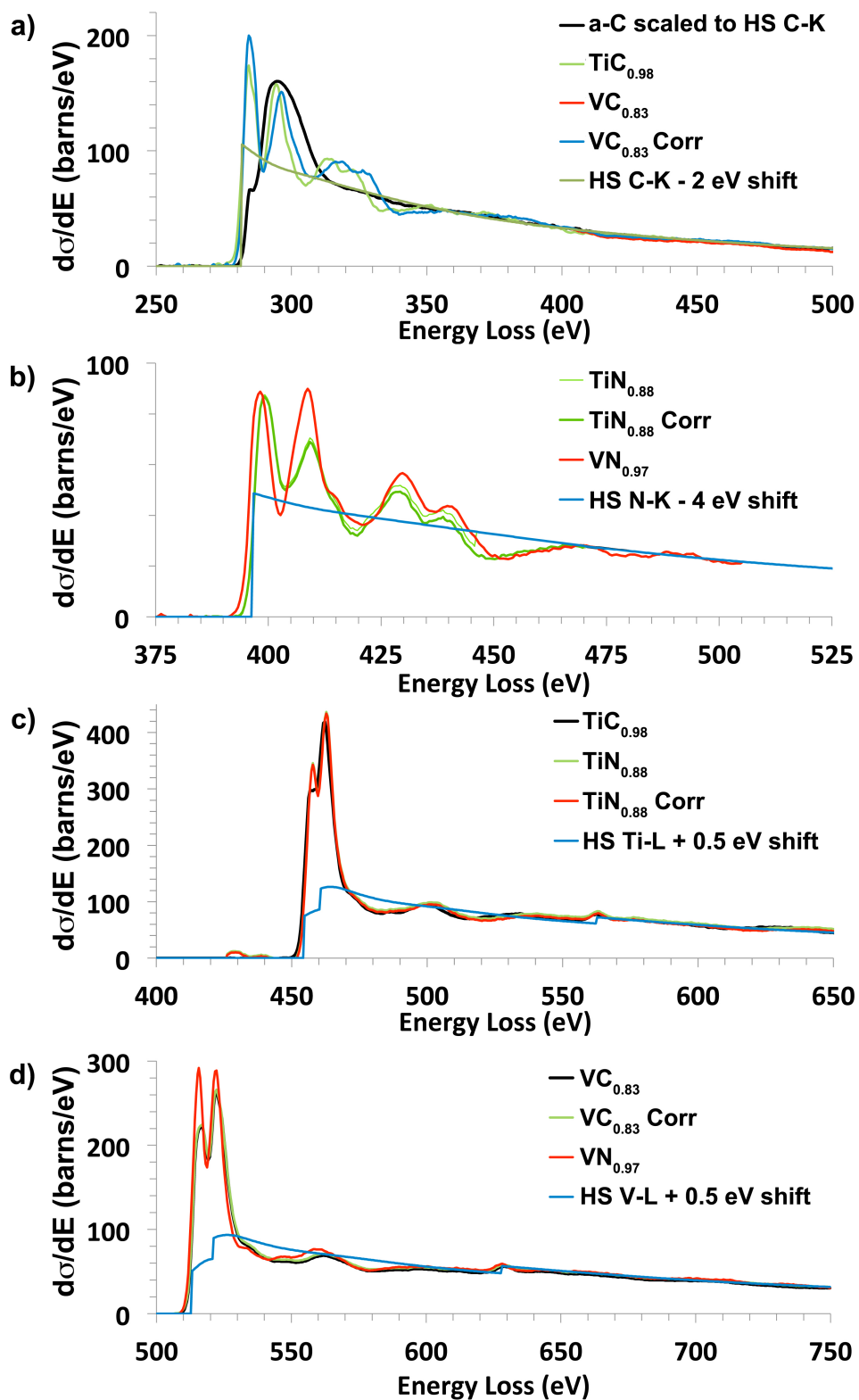

Figure 8 Cross-sections for the individual edges compared to the HS cross-sections. The non-metal cross-sections have been corrected to full stoichiometry and the higher energy

losses are not shown as this is the region extrapolated using the HS cross-section. a) The C K-edge. For comparison, the background subtracted intensity from a thin, amorphous carbon film is shown after scaling to the HS cross-section in the 350 -500 eV range. b) The N K-edge cross-section. c) The Ti L-cross-section. d) The V L-cross-section. Also shown are the effects of small changes to the fits and these changes are discussed in the text.

It is clear that this approach of using experimentally extracted backgrounds for separating the individual cross-sections produces excellent results. Figure 9 looks at the quality of the fits and the implications for quantification using HS cross-sections. Figure 9a considers the fit residuals in more detail. Figures 9b and c show the ratios of the experimental cross-sections to the HS cross-sections for the non-metal and metal cross-sections respectively. Figure 9d shows the results for the "X/M" ratios for stoichiometric MX compounds that are obtained if the experimental cross-sections are analysed using the HS cross-sections. The results shown in Figure 9 suggest that a minor correction to the background fit in some cases would improve the overall consistency in the results.

Whilst the residuals for $TiC_{0.98}$ and $VN_{0.97}$ are close to zero in the atomic regions, those for $VC_{0.83}$ and $TiN_{0.88}$ have non-zero values. Figure 9a shows the deviations for $VC_{0.83}$ with an expanded vertical scale. The thin black line shows that the residuals are negative for ~100eV before the V L-edge and after ~100eV above its threshold and, therefore, that there is a small but significant problem in background fitting for $VC_{0.83}$. The thick black line is after a correction to the background fitting detailed below.

Another way of judging the quality of the agreement is to look at the ratio of the experimental and HS cross-sections. These are shown for the non-metals in Figure 9b and for metals in Figure 9c. In both cases the ratios are plotted as a function of the energy above the edge threshold. For the non-metals, the plots are terminated at the metal edge. The thin lines are the values before the corrections discussed below are made to the $VC_{0.83}$ and $TiN_{0.88}$ cross-sections and the corresponding thick lines include the correction to the background fitting described below. Naturally, all the lines display the effects of the very strong ELNES present on these edges and the degree of overlay of all edges when plotted against energy above threshold is striking. Nevertheless, these plots also show deviations from ideal background fitting. In Figure 9b, the thin black line for the uncorrected C-edge data from $VC_{0.83}$ shows a steady drop at higher losses. This is not the constant value that would be expected if either the stoichiometry or the ideal ratio of experimental and HS cross-sections

27

differed from unity. In Figure 9c, the thin black line for the uncorrected V L-edge from $VC_{0.83}$ data lies below the lines for $TiC_{0.98}$ and $VN_{0.97}$, suggesting problems with the $VC_{0.83}$ background fit, as before. Additionally, the thin green line for the uncorrected $TiN_{0.88}$ data lies above those for $TiC_{0.98}$ and $VN_{0.97}$, suggesting that the background fitting problems for this standard are in the opposite sense. Unfortunately, the limited energy range available for the thin green line for the uncorrected N K-edge from $TiN_{0.88}$ in Figure 9b means that it is difficult to make any judgement about the quality of background fitting for this edge, although based on the poor fitting in Figure 9c, it has to be suspected that there would be a problem here too.
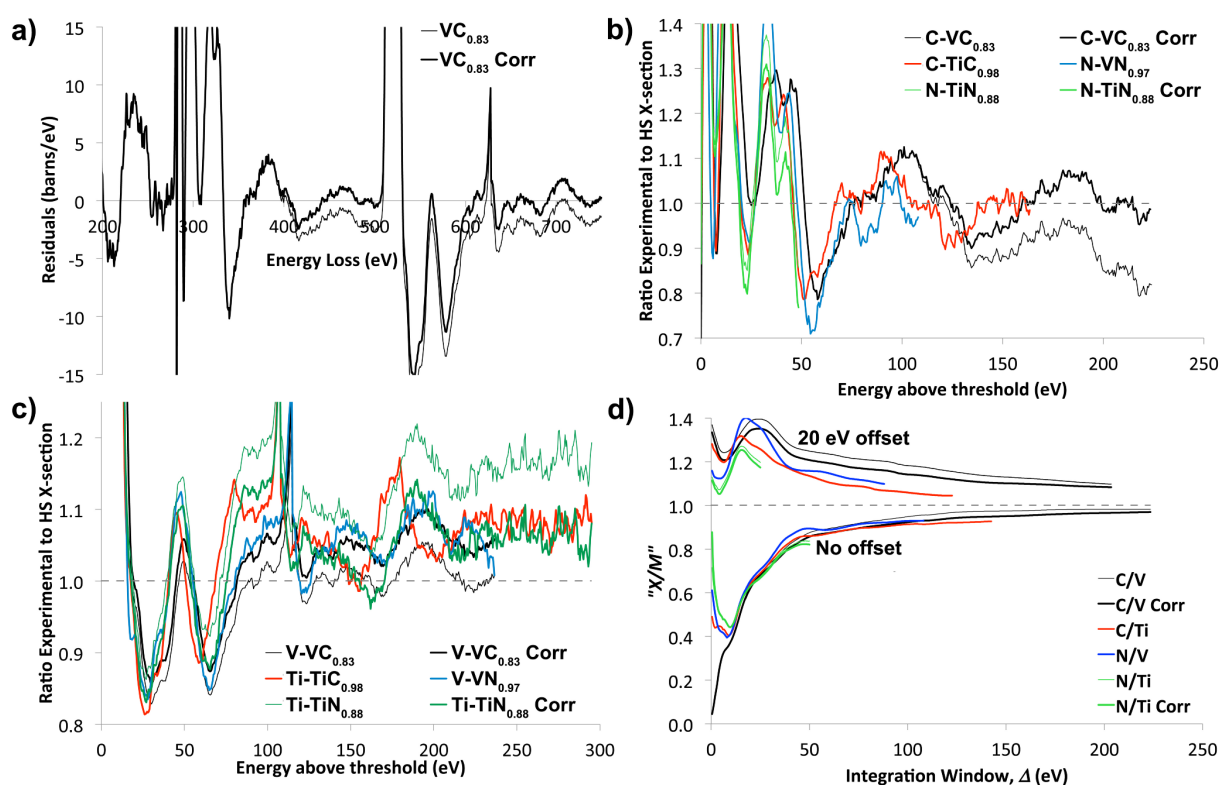

Figure 9 a) The $VC_{0.83}$ residuals shown with an expanded vertical scale. b) The ratio of the experimental non-metal cross-sections, corrected to full stoichiometry, to the corresponding HS cross-sections as a function of energy above threshold. The thin lines are data before correction. c) The ratio of the experimental metal cross-sections to the corresponding HS cross-sections as a function of energy above threshold. The thin lines are data before correction. d) "X/M" versus integration window width, Δ for the stoichiometric standards. The thin lines are data before correction. Two sets of results are shown. For the lower group of plots, the integration window starts at the threshold and, for the upper group, it starts after an offset of 20eV.

One way to judge the implications for quantification is to look at the non-metal to metal ratio, *X/M*, obtained using the traditional quantification process.   Here, the sum of the experimental cross-section over an energy window, *Δ*, is divided by the sum of the HS cross-section over the same window and then the ratio of a value for a non-metal and a metal is taken.   The *X/M* values are shown in Figure 9d as a function of *Δ* and, again, the thin lines are before the corrections.   The maximum value of *Δ* for each compound is set when the window reaches the metal edge threshold.   Two sets of data are shown, one for the integration window starting at threshold and one for the window starting 20eV above the threshold.   In the former case, the window for the experimental data is extended 10eV below threshold to include the signal displaced to lower energy by the finite energy resolution and the point spread function of the detector.

In Figure 9d, the lines obtained with no offset of the integration window group together quite well for window widths greater than 20eV, showing good consistency between them but with the expected effects of ELNES.   Nevertheless, the thin black line for $VC_{0.83}$ is slightly high.   All increase steadily towards unity but, even after an integration window of 220eV, the $VC_{0.83}$ line is still rising and has not reached unity.   If a 20eV offset is used before starting integration, the lines give values greater than unity and are spread over a much wider range of values.   This offset could be increased to exclude more of the ELNES, as recommended by Gatan (instructions in the "Help" file for Digital Micrograph), but this would exclude more of the high intensity signal, which is least susceptible to background error and would also severely limit the possible window width.   Figure 9d clearly illustrates some of the problems of the traditional quantification approach when trying to get accurate compositions because of the sensitivity to integration window width and position.

As the background subtraction is the most problematic area, a simple correction can be applied by returning to the constrained background-fitting concept of Steele et al. [31].   Here, the value of *r* in the extrapolated section of the "experimental background shape" is adjusted to improve the fits for the $VC_{0.83}$ and $TiN_{0.88}$ data.   This results in the thick lines for these compounds in Figures 9b, c, d.   In Figure 8a, the corrected line for $VC_{0.83}$ is shown in blue but is scarcely different from the uncorrected line, showing how small the change is.   In Figure 8b, the corrected line for $TiN_{0.88}$ is shown as a thick green line, which can be distinguished from the uncorrected thin green line.

For $VC_{0.83}$, the change in r is from 2.81 to 3.05 and this brings the deviations close to zero both before and after the V L-edge threshold, as seen in the thick black line in Figure 9a. The corrected experimental to HS cross-section ratios from $VC_{0.83}$, the thick black lines in Figures 9b and c, are in much better agreement with those from $TiC_{0.98}$ and $VN_{0.97}$. In Figure 9d, the *X/M* values are lowered slightly, improving the agreement for the zero offset case.

For $TiN_{0.88}$, the change in r is from 2.81 to 2.41. While it is difficult to comment on the effect on the N cross-section in Figure 9b because of the limited range of energies, the thick green line in Figure 9c is brought into line with the other three. Again, it is difficult to comment on the change of *X/M* in Figure 9d because of the limited energy range.

The change in r for $TiN_{0.88}$ is larger and in the opposite sense to that for $VC_{0.83}$. There is some justification for making the correction for $VC_{0.83}$ in that it corrects both edges at the same time. There is less justification for making the correction for $TiN_{0.88}$ because the energy range available for the N K-edge does not allow an improvement to be demonstrated for it. It is also not clear why what has been taken as the "experimental background shape" has to be corrected. Nonetheless, the overall consistency between all the results is improved if this correction is made.

Turning to the agreement between the experimental and HS cross sections, the ratios for the non-metal cross-sections from $TiC_{0.98}$ and $VC_{0.83}$ in Figure 9b tend to unity at higher losses. Making the assumption that the integrated EXELFS averages to zero in the range above 100eV from the threshold to the metal threshold, the average ratio of the experimental and HS cross-sections can be found. For the C cross-section from $TiC_{0.98}$ this is 0.98(0). For the corrected $VC_{0.83}$ it is 1.00(6). The energy ranges available for $VN_{0.97}$ and $TiN_{0.88}$ do not allow sensible averages to be taken. It is difficult to give errors for the values from $TiC_{0.98}$ and $VC_{0.83}$ owing to the oscillations from the fine structure and the uncertainty in the exact composition of the $VC_{0.83}$. However, it is likely to be in range 2-3% and so these two values may well be in agreement. Their average is 0.99.

In the same way, the average for the metal cross-sections in Figure 9c can be calculated. In this case, the window used to calculate the averages starts 120eV above threshold to avoid the L_1 edges and is taken to the end of the dataset at 750eV. The ratios for Ti in $TiC_{0.98}$ and $TiN_{0.88}$ are 1.00(4) and 1.02(0) respectively, giving an average of 1.01. The ratios for V in $VC_{0.83}$ and $VN_{0.97}$ are 1.00(2) and 1.00(9) respectively, giving an average of 1.01. The overall average for the metals is 1.01. The uncertainties in these values are hard to

specify both because of the EXELFS and, for $VC_{0.83}$ and $TiN_{0.88}$, because of the nature of the correction.   Nonetheless, there is considerable overall self-consistency and so it is likely to be 1 or 2%.

e.   Systematic errors

There are many possible sources of systematic error in the determination of the absolute experimental differential cross-sections and the associated inelastic mean free paths.   Here they are looked at in the order they are come across when performing the experiments and processing the data.

The $TiN_{0.88}$, $TiC_{0.98}$ and $VN_{0.97}$ standards were supplied with measured stoichiometries but no errors were given.   In the work by Lengauer et al. [44], the errors typically quoted better 0.1wt% (e.g. Lengauer *et al.* [44]).   The VC sample was supplied as high carbon but without an analysis.   Selected area diffraction analysis showed that it is in the V_6C_5 phase field.   From the phase diagram given by Billingham et al. [34], the minimum possible value of x is ~0.77 and the maximum ~0.85.   The former value is only found for very low processing temperatures.   The most likely value is 0.83 and the uncertainty is probably ±0.02. In addition, there could be some inhomogeneity within the material.   Nonetheless, the results from regions separated by microns are in good agreement and there is good consistency between the individual measurements and so this is not a significant issue.

While the magnification, probe angle and collection angle are carefully calibrated, these calibrations are based on measurements for electrons with no energy loss.   Chromatic effects in the post-specimen optics will make the collection angle a function of energy loss and the changes will depend on the camera length chosen [45].   Since the same conditions are used for the steels and the standards, such effects will cancel out when quantifying the steel data.   However, if significant, they will affect the comparisons of the experimental and calculated cross-sections.   Also, if these experimental cross-sections are used to analyse data taken on an instrument with different electron optics, they could result in an error. Preliminary measurements show that the collection half angle of 36mrad for elastic electrons becomes 36.1, 36.4 and 36.9 mrad for energy losses of 250, 500 and 750eV, respectively.   As a result, the differential HS cross-section of the C K-edge increases by 0.06, 0.6 and 1.8% for these three energies, giving an idea of the absolute error involved from this effect.   Thus the

mean ratio of the experimental to the HS cross-section is likely to decrease from ~0.99 to ~0.98 for the non-metal K-edges and from ~1.01 to ~0.99 for the metal L-edges.

The gain linearity of the detection system is good and the ratio of the signals in the high loss and low loss channels is given accurately by the ratio of the integration times. However, stray scattering contributes to the signals so that the splice ratio differs from the time ratio. By keeping the time ratio at typically 25, the difference is less than 10%. Using the splice ratio gives a smooth join and allows Fourier logarithmic deconvolution but requires a correction to the high loss region intensity in order to extract the cross-section. Thus there is a perturbation in the region of the splice point. However, this is sufficiently far from the carbon K-edge cross-section for there to be no issue.

Surface oxidation and amorphous carbon growth are both potential sources of error. However, the processing seems to deal very effectively with such layers if they are spatially homogeneous but a spatially inhomogeneous layer of the carbon would be a problem. Developments in specimen preparation and pre-treatment have significantly reduced the level of both effects in the final data for the cross-sections and so this will not introduce any significant systematic error.

Electron channelling effects are assumed to be absent as the specimens are extracted in arbitrary directions from random polycrystalline materials. Should the orientation by chance end up close to a low index pole, there could be an effect from channelling. However, the self-consistency over all the edges measured suggest that channelling is not a significant effect. However, it is an area worthy of a more detailed study in the future.

For the extraction of the cross-sections and the inelastic mean free path, the analysis in Section 2 fails for values of t/λ <~0.2 or >~1.0. It is assumed that the former limit is due to surface effects being dominant. The latter is assumed to be due to a failure of the Fourier-logarithmic deconvolution process or to differences arising between the elastic contrast in the zero-loss map used to normalise the loss image and the actual contrast in that loss image. Any residual effects of this type in the thickness range of $0.2 < t/\lambda < 1.0$ are assumed to be small but no attempt has been made to quantify them apart from noting that the fits to the data are good.

The value of λ_B is determined directly for $TiC_{0.98}$ using t and t/λ measured on the same sample using methods that exclude the effects of surface layers. Only the low-loss region of the spectrum is used and the growth of carbon contamination is not a major problem. As expected, the region at the tip of the needle must be excluded as it is dominated by the surface

layer and there may be no bulk material.   For $t/\lambda > 1.0$, the lines of t and t/λ diverge and this region is also excluded.   The region used gives very good straight-line plots but sources of bias may exist here.   Again, these have not been explored in detail.   The use of the Iakoubovskii parameterisation [29] may also be a source of error but the self-consistency of the results suggests that this could only be a small effect.

The biggest sources of systematic error are found when removing the background and separating the edges.   The backgrounds in front of the non-metal edges show significant departures from a power law due to the EXELFS from the metal M-edges.   The use of an "experimental" background shape derived from the $TiN_{0.88}$ has lowered this error considerably.   However, there is no good explanation of why it needs to be adjusted in some cases other than it improves the self-consistency of the results as a whole.

Once the non-metal cross-sections are extrapolated under the metal edges, knowledge of their ELNES/EXELFS is lost and so there is a systematic error in both the metal and the non-metal cross-sections.   This is particularly significant for $TiN_{0.88}$, where the N and Ti edges are close together.   It can be reduced by using the shape extracted from the $VN_{0.97}$ to make a correction.   However, the metal cross-sections are large at this point and consequently the error in them will be small.

In principle, it would be possible to extend this procedure to a wide range of other materials and EELS edges provided that (i) a well-characterised standard can be prepared, (ii) a robust background subtraction procedure can be found, (iii) the edges are reasonably well separated.   The application of this kind of procedure becomes rather more difficult for very low energy EELS edges, as will both suffer from complex backgrounds on the tail of the plasmon peak and there will be several edges all overlapping in this region.   Thus, the $M_{2,3}$ edges for V or Ti would be extremely difficult to use for quantitative and robust quantification. This "difficult" region extends to at least ~ 200 eV due to EXELFS from low lying edges and ongoing work at Glasgow shows that background subtraction on the Nb $M_{4,5}$ edge (nominally at 205 eV) on Nb carbides can be difficult. Nevertheless, for other edges lying above this range, we expect this method to be of widespread applicability.

5.   CONCLUSIONS

Highly successful methods of measuring the experimental inelastic mean free path and the differential cross-section using DualEELS have been demonstrated.   Both methods deal

with the effects of surface layers and the method for the mean free path deals with non-ideal shape of the needle specimen.

The inelastic mean free path for $TiC_{0.98}$ is found to be 103.6±0.5nm compared to 126.9nm predicted by the Iakoubovskii parameterisation. However, from the overall self-consistency of the results, the relative values from the parameterisation appear to be accurate.

The cross-sections extracted from the experimental data have precisions of ~1%. Removing the background and separating out the individual cross-sections is difficult. The most effective method found uses an "experimental" background shape extrapolated with a power law, although minor corrections are needed in some case to produce the most self-consistent results.

It is found that despite the large convergence and collection angles used in the work, channelling can still have a small effect (<5%) on the measured cross sections, so for best precision it is desirable to avoid a strong channelling condition.

Using the known (or inferred) stoichiometry of the standards to correct the non-metal cross-sections to full stochiometry is very successful. These together with the metal cross-sections provide an accurate method of quantifying binary, ternary and quaternary compounds of C, N, Ti and V, avoiding the issues and errors associated with methods based on calculated HS cross-section. They will be used in a subsequent paper to quantify data from precipitates in steels extracted by the methods reported in a previous paper [1].

The experimental results agree well with the HS cross-sections in the atomic region well above threshold. The average ratio between the experimental and HS cross-sections in this region is 0.99 for the non-metal cross-sections or 0.98 if the correction for chromatic effects is correct, and 1.01 for the metals or 0.99 if the correction for chromatic effects is correct. It is difficult to give estimates of either their precision or accuracy but both are likely to be in the range of a few per cent given the narrow range within which the values for all the edges lie. This agreement is much closer than previously reported where it is typically said to be ~5% for the non-metal K-edges and 15% for the metal L-edges. The explanation for the improved agreement is likely to be that the ratio is calculated further above threshold in this work, which clearly shows the effects of the ELNES and EXELFS is significant up to at least ~100eV beyond the threshold.

6. ACKNOWLEDGEMENTS

REFERENCES

1.	Bobynko, J., I. MacLaren, and A.J. Craven, *Spectrum imaging of complex nanostructures using DualEELS: I. digital extraction replicas.* Ultramicroscopy, 2015. **149**: p. 9-20.
2.	Scott, J., et al., *Near-simultaneous dual energy range EELS spectrum imaging.* Ultramicroscopy, 2008. **108**(12): p. 1586-1594.
3.	Gubbens, A., et al., *The GIF Quantum, a next generation post-column imaging energy filter.* Ultramicroscopy, 2010. **110**(8): p. 962-970.
4.	Johnson, D.W. and J.C.H. Spence, *DETERMINATION OF SINGLE-SCATTERING PROBABILITY DISTRIBUTION FROM PLURAL-SCATTERING DATA.* Journal of Physics D-Applied Physics, 1974. **7**(6): p. 771-780.
5.	Egerton, R.F., *Electron Energy-Loss Spectroscopy in the Electron Microscope*. 2011, New York: Springer.
6.	Paul, G., et al., *Erste Erkenntnisse zum Ausscheidungsverhalten von Mikrolegierungselementen in Hoch-Mangan Stählen*, in *Metallographie-Tagung*, G.n. Petzow, Editor. 2012, DGM: Rostock.
7.	Bobynko, J., et al., *Nanocharacterisation of precipitates in austenite high manganese steels with advanced techniques: HRSTEM and DualEELS mapping.* Electron Microscopy and Analysis Group Conference 2013 (Emag2013), 2014. **522**.
8.	Leapman, R.D., P. Rez, and D.F. Mayers, *K-SHELL, L-SHELL AND M-SHELL GENERALIZED OSCILLATOR-STRENGTHS AND IONIZATION CROSS-SECTIONS FOR FAST ELECTRON COLLISIONS.* Journal of Chemical Physics, 1980. **72**(2): p. 1232-1243.
9.	Egerton, R.F., *VALUES OF K-SHELL PARTIAL CROSS-SECTION FOR ELECTRON ENERGY-LOSS SPECTROMETRY.* Journal of Microscopy-Oxford, 1981. **123**(SEP): p. 333-337.
10.	Egerton, R.F., *OSCILLATOR-STRENGTH PARAMETERIZATION OF INNER-SHELL CROSS-SECTIONS.* Ultramicroscopy, 1993. **50**(1): p. 13-28.
11.	Egerton, R., *Electron Energy-Loss Spectroscopy in the Electron Microscope*. 2011.
12.	Rez, D. and P. Rez, *THE CONTRIBUTION OF DISCRETE TRANSITIONS TO INTEGRATED INNER SHELL IONIZATION CROSS-SECTIONS.* Microscopy Microanalysis Microstructures, 1992. **3**(5): p. 433-442.
13.	Crozier, P.A., et al., *ON THE DETERMINATION OF INNER-SHELL CROSS-SECTION RATIOS FROM NIO USING EELS.* Journal of Microscopy-Oxford, 1987. **148**: p. 279-284.
14.	Hofer, F., P. Golob, and A. Brunegger, *EELS QUANTIFICATION OF THE ELEMENTS SR TO W BY MEANS OF M45 EDGES.* Ultramicroscopy, 1988. **25**(1): p. 81-84.

15. Hofer, F. and P. Golob, *QUANTIFICATION OF ELECTRON ENERGY-LOSS SPECTRA WITH K-SHELL AND L-SHELL IONIZATION CROSS-SECTIONS.* Micron and Microscopica Acta, 1988. **19**(2): p. 73-86.

16. Hofer, F., *EELS QUANTIFICATION OF THE ELEMENTS BA TO TM BY MEANS OF N-45 EDGES.* Journal of Microscopy-Oxford, 1989. **156**: p. 279-283.

17. Manoubi, T., C. Colliex, and P. Rez, *QUANTITATIVE ELECTRON-ENERGY LOSS SPECTROSCOPY ON M45 EDGES IN RARE-EARTH-OXIDES.* Journal of Electron Spectroscopy and Related Phenomena, 1990. **50**(1-2): p. 1-18.

18. Hofer, F., *DETERMINATION OF INNER-SHELL CROSS-SECTIONS FOR EELS-QUANTIFICATION.* Microscopy Microanalysis Microstructures, 1991. **2**(2-3): p. 215-230.

19. Hofer, F. and P. Wilhelm, *EELS MICROANALYSIS OF THE ELEMENTS CA TO CU USING M-23 EDGES.* Ultramicroscopy, 1993. **49**(1-4): p. 189-197.

20. Hofer, F., G. Kothleitner, and P. Rez, *Ionization cross-sections for the L(23)-edges of the elements Sr to Mo for quantitative EELS analysis.* Ultramicroscopy, 1996. **63**(3-4): p. 239-245.

21. Harkins, P., et al., *Quantitative electron energy-loss spectroscopy (EELS) analyses of lead zirconate titanate.* Micron, 2008. **39**(6): p. 709-716.

22. Bach, D., R. Schneider, and D. Gerthsen, *EELS of Niobium and Stoichiometric Niobium-Oxide Phases-Part II: Quantification.* Microscopy and Microanalysis, 2009. **15**(6): p. 524-538.

23. Kuimalee, S., et al., *Quantitative analysis of a complex metal carbide formed during furnace cooling of cast duplex stainless steel using EELS and EDS in the TEM.* Micron, 2010. **41**(5): p. 423-429.

24. Bach, D., et al., *EELS of Niobium and Stoichiometric Niobium-Oxide Phases-Part I: Plasmon and Near-Edges Fine Structure.* Microscopy and Microanalysis, 2009. **15**(6): p. 505-523.

25. Crozier, P.A., *MEASUREMENT OF INELASTIC ELECTRON-SCATTERING CROSS-SECTIONS BY ELECTRON ENERGY-LOSS SPECTROSCOPY.* Philosophical Magazine B-Physics of Condensed Matter Statistical Mechanics Electronic Optical and Magnetic Properties, 1990. **61**(3): p. 311-336.

26. Kothleitner, G., et al., *Linking TEM Analytical Spectroscopies for an Assumptionless Compositional Analysis.* Microscopy and Microanalysis, 2014. **20**(3): p. 678-686.

27. Hofer, F. and B. Luo, *TOWARDS A PRACTICAL METHOD FOR EELS QUANTIFICATION.* Ultramicroscopy, 1991. **38**(2): p. 159-167.

28. Mendis, B.G., M. MacKenzie, and A.J. Craven, *A new analytical method for characterising the bonding environment at rough interfaces in high-k gate stacks using electron energy loss spectroscopy.* Ultramicroscopy, 2010. **110**(2): p. 105-117.

29. Iakoubovskii, K., et al., *Thickness measurements with electron energy loss spectroscopy.* Microscopy Research and Technique, 2008. **71**(8): p. 626-631.

30. Malis, T., S.C. Cheng, and R.F. Egerton, *EELS Log-Ratio Technique for Specimen-Thickness Measurement in the TEM.* Journal of Electron Microscopy Technique, 1988. **8**(2): p. 193-200.

31. Zhang, H.-R., R.F. Egerton, and M. Malac, *Local thickness measurement through scattering contrast and electron energy-loss spectroscopy.* Micron, 2012. **43**(1): p. 8-15.

32. Lengauer, W. and P. Ettmayer, *PHYSICAL AND MECHANICAL-PROPERTIES OF CUBIC DELTA-VN1-X.* Journal of the Less-Common Metals, 1985. **109**(2): p. 351-359.

33. Venables, J.D., D. Kahn, and R.G. Lye, *STRUCTURE OF ORDERED COMPOUND V6C5.* Philosophical Magazine, 1968. **18**(151): p. 177-&.

34. Billingham, J., P.S. Bell, and M.H. Lewis, *VACANCY SHORT-RANGE ORDER IN SUBSTOICHIOMETRIC TRANSITION-METAL CARBIDES AND NITRIDES WITH NACL STRUCTURE .1. ELECTRON-DIFFRACTION STUDIES OF SHORT-RANGE ORDERED COMPOUNDS.* Acta Crystallographica Section A, 1972. **A 28**(NOV1): p. 602-606.

35. Singh, D.R.P., N. Chawla, and Y.L. Shen, *Focused Ion Beam (FIB) tomography of nanoindentation damage in nanoscale metal/ceramic multilayers.* Materials Characterization, 2010. **61**(4): p. 481-488.

36. McCaffrey, J.P. and J.M. Baribeau, *A TRANSMISSION ELECTRON-MICROSCOPE (TEM) CALIBRATION STANDARD SAMPLE FOR ALL MAGNIFICATION, CAMERA CONSTANT, AND IMAGE/DIFFRACTION PATTERN ROTATION CALIBRATIONS.* Microscopy Research and Technique, 1995. **32**(5): p. 449-454.

37. Egerton, R.F., *FACTORS AFFECTING THE ACCURACY OF ELEMENTAL ANALYSIS BY TRANSMISSION EELS.* Microscopy Microanalysis Microstructures, 1991. **2**(2-3): p. 203-213.

38. Zaluzec, N.J. in *38th Annual Proceedings: Electron Microscopy Society of America*. 1980. Claitor's.

39. Goldschmidt, H.J., *Interstitial Alloys*. 1957, London: Butterworths.

40. Lucas, G., et al., *Multivariate statistical analysis as a tool for the segmentation of 3D spectral data.* Micron, 2013. **52-53**: p. 49-56.

41. Steele, J.D., Titchmarsh, J.M., Chapman, J.N. and Paterson, J.H., Ultramicroscopy, 1985. **17**, p. 273-276.

42. Ahn, C.C. and P. Rez, *INNER SHELL EDGE PROFILES IN ELECTRON-ENERGY LOSS SPECTROSCOPY.* Ultramicroscopy, 1985. **17**(2): p. 105-115.

43. Paxton, A.T., et al., *The near-edge structure in energy-loss spectroscopy: many-electron and magnetic effects in transition metal nitrides and carbides.* Journal of Physics-Condensed Matter, 2000. **12**(5): p. 729-750.

44. Lengauer, W., et al., *Solid-State Properties of Group Ivb Carbonitrides.* Journal of Alloys and Compounds, 1995. **217**(1): p. 137-147.

45. Craven, A.J. and T.W. Buggy, *DESIGN CONSIDERATIONS AND PERFORMANCE OF AN ANALYTICAL STEM.* Ultramicroscopy, 1981. **7**(1): p. 27-37.